Computer Physics Communications 315 (2025) 109694

Contents lists available at ScienceDirect

Computer Physics Communications

journal homepage: www.elsevier.com/locate/cpc

Computational Physics

# *Semtex*: Development and application of the solver methodology for incompressible flows with generalized Newtonian rheologies

H.M. Blackburn [a,*], M. Rudman [a], J. Singh [a,b]

[a] Department of Mechanical and Aerospace Engineering, Monash University, Vic 3800, Australia
[b] Department of Aerospace Engineering, University of Michigan, Ann Arbor, MI 48109, USA

ARTICLE INFO

The review of this paper was arranged by Prof. Peter Vincent

*Keywords:*
Navier–Stokes
Non-Newtonian
Generalized Newtonian rheology
Spectral elements
Cylindrical coordinates
Direct numerical simulation

ABSTRACT

The methodology for simulation of incompressible flows with generalized Newtonian viscosity models, for example shear-thinning rheologies, within the *Semtex* framework of open-source spectral-element/Fourier flow solvers [1,2] is outlined. Direction is given regarding the rheology models employed and how appropriate parameters are derived and supplied to the solver. Exponential spatial convergence of solutions is demonstrated for both Cartesian and cylindrical geometries. Other example applications deal with DNS of turbulent flows in pipes. We use *Semtex* to highlight the central importance of adequate rheology characterization for accurate simulation of turbulent flows of generalized Newtonian fluids.

## 1. Introduction

*Semtex* is a well-validated open-source framework of spectral element computer codes that are mainly directed at high-performance direct numerical simulation (DNS) of incompressible flows. Domain geometries accommodated are two-dimensional Cartesian (using structured or unstructured conforming quadrilateral meshes), with three-dimensional geometries possible by extrusion in an orthogonal coordinate, on the assumption of periodicity and Fourier expansions in that direction, see Fig. 1. The orthogonal coordinate may be chosen as Cartesian or cylindrical. Thus, flows accommodated may be two- or three-component and two- or three-dimensional, in either Cartesian or cylindrical coordinate systems. Solver speed is high, largely through the default adoption of direct elliptic solvers using element-level static condensation for both pressure and velocity components, and parallel solution of Fourier modes (either singly or as sets) is possible with MPI, allowing further speed-up for three-dimensional solutions. Exponential convergence of solutions in cylindrical coordinates with respect to number of points along an element edge was established in [3], while earlier work with a related solver [4] showed that convergence was also exponential in Cartesian coordinates. Numerical, scaling, implementation, convergence and usage details within the *Semtex* framework for incompressible flows with Newtonian rheologies were detailed in [1]. A notable performance feature documented there is that for DNS of three-dimensional problems, speed-up generally increases linearly with number of CPUs until the workload becomes dominated by communication overheads; depending on the particulars of the mesh used, this limit could be many hundreds or thousands of processors. The source code package is available on `Gitlab` [2]; top-level routines are written in C++, with some lower-level library routines provided in both C and Fortran.

While Newtonian rheologies i.e. those with a constant viscosity are almost standard in DNS studies, non-Newtonian rheologies are important in many applications areas, from industrial through biological to geophysical flows. In the present work, our focus is on DNS of incompressible flows of fluids with generalized Newtonian (GN) rheologies, for which the viscosity taken to be locally and instantaneously dependent on the magnitude of the strain rate. Other types of non-Newtonian fluids include viscoelastic, thixotropic and rheopeptic rheologies, see [5,6]. While GN is conceptually the simplest non-Newtonian rheology, it is technologically relevant with a wide range of applicability, for example in modelling of high-concentration mining tailings streams and flows in petroleum drill strings [7,8], but also in modelling blood flows [9–11].

Given the fluid velocity vector $\boldsymbol{u}(\boldsymbol{r},t)$ and the rate of strain tensor $\boldsymbol{S}=[\boldsymbol{\nabla u}+(\boldsymbol{\nabla u})^{\mathrm{T}}]/2$, the viscosity $\mu$ is taken to be a scalar function of $\dot{\gamma}=(2\boldsymbol{S}:\boldsymbol{S})^{1/2}$, the magnitude (second invariant) of $\boldsymbol{S}$, i.e. $\mu=\mu(\dot{\gamma})$.

* Corresponding author.
*E-mail address:* hugh.blackburn@monash.edu (H.M. Blackburn).

https://doi.org/10.1016/j.cpc.2025.109694
Received 23 December 2024; Received in revised form 23 May 2025; Accepted 28 May 2025
Available online 5 June 2025

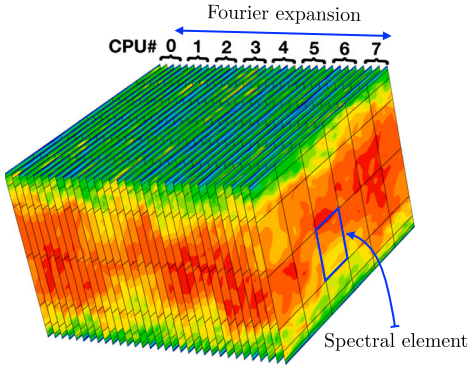


**Fig. 1.** Indication of a possible spatial and computational domain style for *Semtex* with a three-dimensional spectral element/Fourier discretization. The Fourier expansion coordinate may be either cylindrical or Cartesian, and one or more Fourier modes (pairs of spatial planes) may reside on a processor, with parallel execution enabled using MPI across modes. While the two-dimensional spectral element mesh shown is structured, unstructured meshes may also be used.

As for Newtonian fluids, the shear stress $\boldsymbol{\tau}$ is twice the product of the viscosity and rate of strain tensor,

$$\boldsymbol{\tau} = 2\mu(\dot{\gamma})\boldsymbol{S}, \tag{1}$$

but since now $\mu$ is now a function of $\boldsymbol{S}$, this relationship is nonlinear, unlike the situation in Newtonian fluids. Common instances of GN rheologies $\mu(\dot{\gamma})$ are: power law, Herschel–Bulkley, Carreau–Yasuda and Cross, see §4 below for details. Despite the apparent conceptual simplicity of GN rheology, the added complexity means that there are fewer analytical (and perforce laminar) solutions available for flows of GN fluids than is the case for Newtonian flows; we will introduce some of these solutions when discussing code validation in §5.

Just as for Newtonian fluids, no analytical solutions exist for turbulent flow of generalized Newtonian fluids (GNFs), and without physical experiments, one must resort to DNS, large eddy simulation (LES) or turbulence modelling for predictions.

Direct numerical simulation of the turbulent flow of non-Newtonian fluids was first presented in a series of papers [12–15] that considered the flow of high Reynolds number, weakly viscoelastic fluids in a channel with the aim of investigating drag reduction in surfactant solutions. A psuedo-spectral method was used with 2nd-order time-stepping.

Despite GNFs being significantly easier to model mathematically than viscoelastic fluids, the application of DNS to GNFs was first presented in [16], somewhat later than the viscoelastic studies mentioned above. That work, undertaken with the *Semtex* spectral element/Fourier package, investigated the turbulent flow of power law fluids in a circular pipe. Subsequent to [16], various different methods have been used to undertake DNS of GN flows including finite difference (FD), finite volume (FV) and low-order finite element method (FEM) approaches.

Frequently, in-house codes developed by research groups have been based on FD or, more often, FV methods. They have usually been applied to simple geometries such as channels and pipes. DNS were undertaken in [17] using a 4th-order in space, 2nd-order in time Adams–Bashforth FD scheme for power law and Casson rheology models in a channel geometry. The outcomes were used primarily to provide data for validation of new sub-grid scale models for LES modelling. A more common approach than FD has been the use of FV methods and several in-house codes have been developed based on 2nd-order-in-space-and-time schemes. Two examples are the SIMPLE-based algorithm of [18] used to develop RANS closures for power law fluids from DNS data and the centred difference, Crank–Nicholson code used in [19] to investigate near-wall structures in turbulent channel flow of a Carreau fluid rheology. Higher order schemes have also been used, e.g. 3rd-order in space QUICK scheme with 2nd-order backward Euler method in [20]. In that study, the code was coupled to an immersed boundary method to investigate the effect of surface roughness in turbulent channel flow of a Herschel–Bulkley fluid.

The open source, FV-based software OpenFOAM has also been used to investigate turbulent flow of GNFs, typically with 2nd-order in space and time schemes. Zheng et al. [21] compared OpenFOAM results for a turbulent pipe flow of a Herschel–Bulkley fluid to those obtained with *Semtex*. They showed that although mean flow statistics were only a few percent different between the methods, 2nd-order statistics could vary by as much as 16%. They state that this level of accuracy is perhaps acceptable for engineering calculations, however it likely precludes OpenFOAM use for more fundamental studies of GNF turbulence. Additionally, the optimal CPU time required for an OpenFOAM simulation was approximately 10–15 times longer per grid point than that required for a *Semtex* simulation. Given the fact that spectral element codes typically provide higher resolution per grid point than low-order methods, the compute time required for a given level of accuracy should be much higher with OpenFOAM than with *Semtex*. Other OpenFOAM DNS of turbulent GNFs include those in [22] for turbulent channel flows of power law and Herschel–Bulkley fluids and [23] for turbulent flow of Herschel–Bulkley fluids in a Taylor–Couette geometry.

More geometrically flexible finite element methods have also been used to undertake DNS of GNFs. A 2nd-order-in-space-and-time FEM code was used to simulate onset of instability, transition and flow unsteadiness in patient-derived models of arterial flow assuming a Carreau–Yasuda blood rheology model in [24]. An open-source FEM code [25] was used in [26] to investigate transition in stenotic flow use a modified Cross rheology model. No GN implementation details were provided for these studies. More recently, stabilized FEM methods have been used to consider unsteady flow in stenoses [27] and the discontinuous Galerkin FEM code `ExaDG` has been used to simulate unsteady aortic flow [28]. Both [27] and [28] assumed a Carreau model for blood. Fully turbulent flow simulations of GNFs using FEM, however, appear to be absent.

Recently NEK5000 [29], another spectral element (high-order FEM) code framework, was used in [30] to investigate near-wall back-flow in the turbulent pipe flow of power law fluids. Details of the GN implementation or other possible rheologies were not provided. We note that the fully-implicit methodology used in NEK5000 to deal with non-Newtonian stress-divergence terms differs somewhat from that used in *Semtex*, which takes a simpler semi-implicit approach, as we shall outline in §§2 and 3.

Direct numerical simulation of GNF flows is the focus of the numerical method described in this work. Our solver is implemented within the *Semtex* spectral-element/Fourier code framework [1,2] and has been the basis of a number of research publications dealing mainly with DNS of turbulent flow of GNFs in pipes and related simple geometries [16,21,31–37]. Compared to many other methods that have been used to undertake DNS of GNFs, *Semtex* has the advantage of high spatial accuracy and rapid parallel execution, being at least one order of magnitude faster than the common open source OpenFOAM finite volume code. It is ideal for DNS of flows with two-dimensional geometric complexity and one periodic dimension. Although *Semtex* has been applied to turbulent flows of GNFs for some time, details of the GN solver have not been previously documented, nor have the breadth of available rheology models and applications. Our purpose here is to remedy this situation and describe its use in both standard and more general geometries, to allow users to more readily benefit from application of the GN solver recently included in the open-source distribution [2].

## 2. Methodology

The incompressible Navier–Stokes equations with constant density and a (possibly variable) scalar dynamic viscosity are

$$\rho\frac{\mathrm{D}\boldsymbol{u}}{\mathrm{D}t} = -\nabla p + \boldsymbol{\nabla}\cdot(2\mu\boldsymbol{S}) + \rho\boldsymbol{f}, \text{ with } \boldsymbol{\nabla}\cdot\boldsymbol{u} = 0. \tag{2}$$

If $\mu = \text{const.}$ (and dividing through by $\rho$) this can be simplified in the conventional form

$$\frac{\mathrm{D}\boldsymbol{u}}{\mathrm{D}t} = -\nabla P + \nu\nabla^2\boldsymbol{u} + \boldsymbol{f}, \text{ with } \boldsymbol{\nabla}\cdot\boldsymbol{u} = 0. \tag{3}$$

In timestepping (3) for DNS using a splitting scheme, it is very usual to deal with the nonlinear parts $\boldsymbol{N}$ of $\mathrm{D}\boldsymbol{u}/\mathrm{D}t = \partial_t\boldsymbol{u} + \boldsymbol{N}(\boldsymbol{u})$ explicitly in time (with a timestep restriction chosen to avoid CFL-type instabilities), but to use an implicit method to deal with the viscous terms $\nu\nabla^2\boldsymbol{u}$ (see e.g. [1]), such that the more restrictive viscous instability does not constrain the timestep size.

However, for GNFs, one has instead to deal with viscous terms in the stress-divergence form $\boldsymbol{\nabla}\cdot(2\nu(\dot\gamma)\boldsymbol{S})$, as shown for (2), which will re-introduce the viscous timestep restriction if wholly dealt with explicitly in time. A simple expedient first introduced by Leslie and Gao [38] in the context of Smagorinksy-type LES is to split the viscosity into a constant 'reference' part $\nu_{\text{ref}}$ and a remainder which varies in space and time. This makes

$$\boldsymbol{\nabla}\cdot(2\nu\boldsymbol{S}) = \nu_{\text{ref}}\nabla^2\boldsymbol{u} + \boldsymbol{\nabla}\cdot(2[\nu(\dot\gamma) - \nu_{\text{ref}}]\boldsymbol{S}). \tag{4}$$

One then treats the part $\nu_{\text{ref}}\nabla^2\boldsymbol{u}$ implicitly in time, and lumps $\boldsymbol{\nabla}\cdot(2[\nu(\dot\gamma) - \nu_{\text{ref}}]\boldsymbol{S})$ in with the nonlinear terms $\boldsymbol{N}$ to be dealt with explicitly in time. In practice this methodology often produces an acceptably large timestep (of the same order as that indicated by the CFL limit) and is the basis of our DNS studies of turbulent GN flows cited above.

There is still a problem in selecting a suitable value of $\nu_{\text{ref}}$, since if too large, another type of instability (associated with unphysical negative viscosity) can arise, while if too small, the conventional numerical instability associated with explicit treatment of viscous terms will be re-asserted. In practice, however, finding a suitable balance by trial and error has worked reasonably well. The accuracy of simulations seems relatively insensitive to the exact value of $\nu_{\text{ref}}$ provided stable simulations are obtained (see e.g. Fig. 3 and associated text). Typically, $\nu_{\text{ref}}$ will be chosen to represent an approximate average value of viscosity for the problem at hand. E.g. for a shear thinning fluid where the viscosity at the wall may be assessed based on known wall shear stresses, $\nu_{\text{ref}} \sim 3\nu_{\text{wall}}$ could be an appropriate guess. (For the example given in §8 we have used $\nu_{\text{ref}} = 5\nu_{\text{wall}}$, while for the example in §5.2 where the maximum viscosity is known at the centreline, we have used $\nu_{\text{ref}} = 0.5\nu_{\text{max}}$.) The splitting (4) has some limitations, and does not always allow successful simulation when rheology departs very significantly from Newtonian — e.g. where shear-thinning/thickening is a very dominant effect, or where a significant portion of the flow would in reality move as an unyielded plug.

While it is possible to deal with $\boldsymbol{\nabla}\cdot(2\nu\boldsymbol{S})$ in other ways which are potentially more tractable (and stable) — such as the fully-implicit treatment of [29] or the alternative implicit-explicit treatment of [39] — those methods require iterative solutions, whereas (4), which retains a standard Laplacian term with a constant viscosity, allows us to use direct elliptic solvers. These are fast, and the setup cost is only incurred once, at the commencement of run-time. For three-dimensional problems, each Fourier mode is solved separately, and typically for the linear substeps, concurrently.

## 3. Implementation details

As more fully described in [1] temporal integration used by the `dns` solver in *Semtex* is handled using a 'stiffly-stable' approximation for the derivative of scalar variable $u$ at time level $(n+1)$, based on backwards differencing in time

$$\partial_t u^{(n+1)} \approx (\Delta t)^{-1}\sum_{q=0}^{K}\alpha_q u^{(n+1-q)} \tag{5}$$

where $\Delta t$ is a constant time step and $\alpha_q$ are a set of weights. For $K = 1$, the method is the backwards/implicit Euler approximation with $\alpha_0 = 1$ and $\alpha_1 = -1$. The approximation (5) has an error $O(\Delta t)^{K+1}$; *Semtex* can be run with $K = 1$, 2, or 3, producing successively smaller errors but carrying the penalties of reduction of the region of stable integration in the complex plane as $K$ increases, and the requirement to store more time levels $u^{(n-q)}$ in order to reach $u^{(n+1)}$. For $K \le 2$, (5) is A-stable [40]; the default value in *Semtex* is $K = 2$.

Substituting (4) and (5) into (3) produces a stiffly-stable fractional step time integration scheme for the incompressible Navier–Stokes equations, modified for GN rheologies:

$$\begin{aligned}\boldsymbol{u}^* = -\sum_{q=1}^{K}\alpha_q\boldsymbol{u}^{(n+1-q)} - \Delta t\sum_{q=0}^{K-1}\beta_q\{\boldsymbol{N}(\boldsymbol{u}^{(n-q)}) - \boldsymbol{f}^{(n-q)} \\ -\boldsymbol{\nabla}\cdot(2[\nu(\dot\gamma^{(n-q)}) - \nu_{\text{ref}}]\boldsymbol{S}^{(n-q)})\},\end{aligned} \tag{6}$$

$$\nabla^2 P^{(n+1)} = (\Delta t)^{-1}\boldsymbol{\nabla}\cdot\boldsymbol{u}^*, \tag{7}$$

$$\boldsymbol{u}^{**} = \boldsymbol{u}^* - \Delta t\boldsymbol{\nabla}P^{(n+1)}, \tag{8}$$

$$\nabla^2\boldsymbol{u}^{(n+1)} - \frac{\alpha_0}{\nu_{\text{ref}}\Delta t}\boldsymbol{u}^{(n+1)} = -\frac{\boldsymbol{u}^{**}}{\nu_{\text{ref}}\Delta t}, \tag{9}$$

where the weights $\alpha_q$ are those introduced in (5), and weights $\beta_q$ are those for explicit polynomial-based extrapolation (at order $K-1$) of values from time levels $(n-q)$ to time level $(n+1)$. Compared to the equivalent equations in [1], new stress-divergence terms appear in (6), and $\nu_{\text{ref}}$ is used in place of $\nu$ in (9).

This fractional-step scheme is an adaptation of the method originally proposed in [41] for the incompressible Navier–Stokes equations. Such schemes were later categorized as velocity-correction methods and given firmer theoretical bases [42,43]. As those works describe, in order to maintain the formal temporal accuracy of the method, it is required to introduce the identity

$$\nabla^2\boldsymbol{u} = \boldsymbol{\nabla}(\boldsymbol{\nabla}\cdot\boldsymbol{u}) - \boldsymbol{\nabla}\times(\boldsymbol{\nabla}\times\boldsymbol{u}) \tag{10}$$

and exploit $\boldsymbol{\nabla}\cdot\boldsymbol{u} = 0$ when deriving boundary conditions for the pressure–Poisson equation (7) from the Navier–Stokes equations (3), leading to the so-called rotational forms of the fractional-step schemes [42,43]. In the present setting, this gives the following approximation for a computed-Neumann pressure boundary condition at time level $(n+1)$, on any boundary where the pressure is not otherwise available (e.g. at walls):

$$\begin{aligned}\partial_n P^{(n+1)} \approx -\boldsymbol{n}\cdot\sum_{q=0}^{K-1}\big[\beta_q\{\boldsymbol{N}(\boldsymbol{u}^{n-q}) - \boldsymbol{f}^{(n-q)} \\ -\boldsymbol{\nabla}\cdot(2[\nu(\dot\gamma^{(n-q)}) - \nu_{\text{ref}}]\boldsymbol{S}^{(n-q)})\} + \nu_{\text{ref}}\boldsymbol{\nabla}\times\boldsymbol{\nabla}\times\boldsymbol{u}^{(n-q)} + \partial_t\boldsymbol{u}^{(n-q)}\big],\end{aligned} \tag{11}$$

where $\boldsymbol{n}$ is the unit outward normal on the domain boundary. Again, compared to the equivalent equation in [1], new stress-divergence terms appear in (11), and $\nu_{\text{ref}}$ is used in place of $\nu$ in the rotational term. Owing to the presence of viscous terms in (11) which are not dealt with using (10) one may be concerned that the temporal accuracy of the method could be compromised. We demonstrate in Appendix A that typically, the method retains the intended formal temporal accuracy when stable outcomes are obtained.

*Semtex* uses equal-order approximations for velocity and pressure variables; in FEM nomenclature, (6)–(9), (11) becomes a $\mathbb{P}_N$–$\mathbb{P}_N$ time-integration scheme. Though one may be concerned about violations of the inf-sup condition with such equal order interpolations, in practice this does not seem to be problematic for high-order methods coupled with the fractional-step/rotational scheme described above, see e.g. [44], §8.3.3.

If the stress-divergence terms are omitted from (6)–(9), (11) and $\nu$ replaces $\nu_{\text{ref}}$, the standard Newtonian algorithm from [1] is obtained, and the DNS solver is called `dns`. To distinguish the GN solver, which is the main focus of what follows, it is instead called `gnewt`. While for the `dns` solver various forms of the nonlinear terms are available, in `gnewt`

only the skew-symmetric form is implemented, i.e. $\boldsymbol{N} = [\boldsymbol{u}\cdot\boldsymbol{\nabla u} + \boldsymbol{\nabla}\cdot(\boldsymbol{uu})]/2$. In our experience, this form is the most numerically robust.

So far as the user is concerned, there is generally little difference between setting up a session file for the DNS solver `dns`, as and the GN solver `gnewt`, as we will show in §§4 and 5. Typically all that is required is the addition of a small number of extra rheology model parameters within the `TOKENS` section of the file, as we will outline below. Regardless of the particular GN rheology chosen, one must set a value for the token `REFVIS`, i.e. $\nu_{\text{ref}}$.

The outputs produced by `gnewt` are very similar to those of `dns`; an exception is that the viscosity is written out to solution files in addition to velocity and pressure fields. A restriction compared to `dns` is that transport of a scalar (and associated possible modelling of buoyancy effects) is not at present implemented in `gnewt`. The performance and scaling characteristics of `gnewt` are nearly identical to those of `dns`, as reported in [1]. A slight overhead is incurred for computation of the extra terms shown in (6) and (11).

## 4. Rheology models

Computation of kinematic viscosity $\nu(\dot\gamma)$ for different rheology models remains to be described. The kinematic viscosity models implemented in the `gnewt` solver are set out below. We note that within the solver, a constant density $\rho = 1$ is assumed, so that viscosities become of kinematic type (with dimensions $\mathrm{L}^2/\mathrm{T}$). However, viscosities provided by rheology models are typically given in dynamic form — dimensions $\mathrm{M}/(\mathrm{LT})$ — we examine techniques for non-dimensionalizing such models for computation in Appendix B.

All the models require the user to define numeric rheology tokens to the `gnewt` solver within the standard `TOKENS` section of an ASCII *Semtex* session file. Such tokens are parsed by the solver and so may be computed based on other tokens previously defined, as we will show below when dealing with validation examples. Values installed for these tokens may be recalled by the user as required, see §4.5 below.

### 4.1. Power law

The power law model

$$\nu = \rho^{-1} K \dot\gamma^{n-1}, \tag{12}$$

where $K$ is the consistency and $n$ is the power-law index, was one of the earliest proposed generalized Newtonian models [5]. While simple to define, it suffers from a numerical singularity where the shear rate falls to zero (e.g. in the centre of a laminar pipe or channel flow), giving an infinite viscosity. It reverts to the conventional Newtonian model for $n = 1$; fluids with $n < 1$ are shear-thinning while those with $n > 1$ are shear-thickening.

In order to use the power law model, the `TOKEN PowerLaw` must be set (to any non-zero value; we typically use `PowerLaw=1`). Also required are values for `PL_N`, i.e. the exponent $n$, and `PL_K` (which, since we are actually setting constants for $\nu$ rather than $\mu$, is technically $\rho^{-1}K$). Optionally the user can set the token `PL_ZERO`, which regularizes the viscosity and is used within the code as a cut-off minimum value for $\dot\gamma$ in order to avoid the possibility of $\nu$ becoming undefined.

### 4.2. Herschel–Bulkley

This allows the modelling of viscoplastic behaviour and may be considered an elaboration of the power law model:

$$\nu = \rho^{-1}[\tau_y/\dot\gamma + K\dot\gamma^{n-1}], \tag{13}$$

where $\tau_y$ is the yield stress. In the restriction $n = 1$, it becomes the Bingham model. As for the power law rheology, it predicts infinite viscosity if the shear rate falls to zero.

In order to use this model, the `TOKEN HB` must be set. Also required are values for `HB_N`, i.e. the exponent $n$, `HB_K` (which again is technically $\rho^{-1}K$), and `YIELD_STRESS`, actually $= \rho^{-1}\tau_y$). Optionally the user can again set a token `HB_ZERO`, which will be used as a cut-off minimum value for $\dot\gamma$.

### 4.3. Carreau–Yasuda

This model has two plateau kinematic viscosities; $\nu_0$ for low shear rates and $\nu_\infty$ for high shear rates, with a power-law type blending for intermediate rates.

$$\nu = \nu_\infty + (\nu_0 - \nu_\infty)[1 + (\lambda\dot\gamma)^a]^{(n-1)/a}. \tag{14}$$

In the restriction $a = 2$ this is known as the Carreau model. The variable $n$ is analogous to the equivalent power-law model variable in that for the power-law blend regime, it describes the slope of $(\nu - \nu_\infty)/(\nu_0 - \nu_\infty)$.

This model does not allow the viscosity to become infinite. The user must set `CAR_YAS`, and provide parameters `CY_LAMBDA`, `CY_A`, `CY_N`, `VISC_ZERO` and `VISC_INF`.

### 4.4. Cross

The Cross model also has two plateau kinematic viscosities for low and high shear rates, with a blend for intermediate rates. Again, infinite viscosities do not arise.

$$\nu = \nu_\infty + (\nu_0 - \nu_\infty)[1 + (\lambda\dot\gamma)^n]^{-1}. \tag{15}$$

The user must set the `TOKEN CROSS`, and provide parameters `CROSS_LAMBDA`, `CROSS_N`, `VISC_ZERO` and `VISC_INF`.

### 4.5. Coding of rheology models

Since the rheology models above all start with pre-computation of $\dot\gamma$, it is fairly straightforward to implement other generalized Newtonian rheologies if required (by modifying file `viscosity.cpp`). In Fig. 2 we show a code extract for computation of viscosity for the Cross rheology model, which uses *Semtex*'s `auxfield` class operator functions. A reader with some understanding of C++ should be able to grasp the connection between this code snippet and (15).

## 5. Laminar validation studies

As noted in §1, there is a limited number of (steady, laminar, two-dimensional) analytical solutions available to allow validation of computations for flows of GNFs. The examples given in this section demonstrate accuracy of the numerical method for steady two-dimensional solutions in both Cartesian and cylindrical coordinates, illustrating that the rheology models and numerical treatment work as expected. Steady solutions were obtained by integrating over sufficient elapsed time. The veracity and performance of the underlying unsteady DNS methodology used by *Semtex* was previously shown in [1].

### 5.1. Taylor–Couette flow of power-law fluid

We commence with an examination of the spatial convergence properties of the methodology for a simple problem that has an analytical solution and which may be computed in either Cartesian or cylindrical coordinates. This is two-dimensional laminar Taylor–Couette flow of power law fluid, $\nu = \rho^{-1}K\dot\gamma^{n-1}$. If $R_i$ and $R_o$ be the inner and outer radii of the domain, rati $\eta = R_i/R_0$, with respective azimuthal speeds $w_i$ and $w_0$, difference $\Delta V = w_i - w_0$, we take $\Omega_i = w_i/(R_i\Delta V)$ and $\Omega_o = w_o/(R_0\Delta V)$. Then the azimuthal velocity as a function of radius $r$ is $w = Ar + Br^{(n-2)/n}$, with constants $A = (\Omega_o - \Omega_i\eta^{2/n})/(1 - \eta^{2/n})$ and $B = ([\Omega_i - \Omega_o]R_i^{2/n})/(1 - \eta^{2/n})$. (With $n = 1$ this reduces

```
    // -- Cross model: GNV = nu_inf + (nu_0-nu_inf)/(1 + (lambda*SR)^N)).

    static const double L      = Femlib::value ("CROSS_LAMBDA");
    static const double N      = Femlib::value ("CROSS_N");
    static const double mu_0   = Femlib::value ("VISC_ZERO");
    static const double mu_inf = Femlib::value ("VISC_INF");
    static const double mu_dif = mu_0 - mu_inf;

    ((*SR *= L ) . pow (N)) += 1.0;
    ((*GNV = mu_dif) /= *SR) += mu_inf;
```

**Fig. 2.** A snippet of C++ code for computation of kinematic viscosity the Cross model, from `Gitlab` distribution file `gnewt/viscosity.cpp`. The strain rate magnitude is input as (a pointer to) a *Semtex* `auxfield` class variable named `SR` and the output ($\nu$) is another `auxfield` variable named `GNV`. Values for the model's `TOKENS` are retrieved from the built-in parser using `Femlib::value` methods. Computation of `GNV` from `SR` proceeds using `auxfield` class operator functions with RPN-like logic. Processing for the other included rheologies proceeds along similar lines, and addition of alternatives proposed by other users should be straightforward.

to the conventional Newtonian solution.) The kinematic viscosity is $\nu = K(2B/n)^{n-1} r^{(2-2n)/n}$.

In *Semtex* one may compute using either Cartesian or cylindrical coordinate systems, see [1,3]. In cylindrical coordinates this problem requires a two-dimensional, three-component (2D3C) computation where only the azimuthal velocity is non-zero, whereas in Cartesian coordinates (with an annular domain) one needs a two-dimensional, two-component (2D2C) computation, the $x$, $y$ components of which are available from the solution above via a coordinate transformation.

Below is a complete listing of a *Semtex* session file used to compute the cylindrical-coordinate results for `N_P=7` (7 points per element edge; polynomial order 6) shown in Fig. 3. Reynolds number has been set low enough that Taylor vortices will not form. We note that in cylindrical coordinates, *Semtex* uses $x$, $y$ and $z$ as the axial, radial and azimuthal coordinates with $u$, $v$ and $w$ as the corresponding velocity components. The example uses the `yacc`-based function parser included in *Semtex* to compute derived constants (`TOKENS`), boundary conditions (`BCS`), and initial/comparison conditions (`USER`) — the latter can be used by the *Semtex* `compare` utility both to compute starting values and to compare against computed outcomes. See [1] and the user guide within the *Semtex* repository at [2] for further explanation.

```
<FIELDS>
  u  v  w  p
</FIELDS>

<TOKENS>
  CYLINDRICAL = 1

  N_P      = 7
  N_Z      = 1
  T_FINAL  = 100
  D_T      = 0.01
  N_STEP   = int(T_FINAL/D_T)
  N_TIME   = 1

  Reynolds = 50

  PowerLaw = 1
  PL_K     = 1.0/Reynolds
  PL_N     = 0.6
  PL_ZERO  = 1e-6
  KINVIS   = PL_K
  REFVIS   = 0.95*KINVIS

  Ri       = 0.52
  Ro       = 1.0
  eta      = Ri/Ro
  Wi       = 1.0
  Wo       = -0.5
  deltaV   = Wi-Wo
  Wi       = Wi/deltaV
  Wo       = Wo/deltaV
  OMi      = Wi/Ri
  OMo      = Wo/Ro
  Numer    = 1-eta^(2/PL_N)
  Expon    = (2-2*PL_N)/PL_N
  A        = (OMo-OMi*eta^(2/PL_N))/Numer)
  B        = (OMi-OMo)*Ri^(2/PL_N)/Numer)
</TOKENS>

<USER>
  u = 0
  v = 0
  w = A*y+B*y^(1-2/PL_N)
  p = 0
  l = PL_K*(2*B/PL_N)^(PL_N-1)*y^Expon
</USER>

<GROUPS NUMBER=2>
  1    v    given
  2    w    wall
</GROUPS>

<BCS NUMBER=2>
  1   v   4
      <D>  u = 0.0                    </D>
      <D>  v = 0.0                    </D>
      <D>  w = A*y+B*y^(1.0-2/PL_N)   </D>
      <H>  p                          </H>
  2   w   4
      <D>  u = 0.0                    </D>
      <D>  v = 0.0                    </D>
      <D>  w = A*y+B*y^(1.0-2/PL_N)   </D>
      <H>  p                          </H>
</BCS>

<NODES NUMBER=9>
    1    0      0.52    0
    2    0.5    0.52    0
    3    1      0.52    0
    4    0      0.76    0
    5    0.5    0.76    0
    6    1      0.76    0
    7    0      1       0
    8    0.5    1       0
    9    1      1       0
</NODES>

<ELEMENTS NUMBER=4>
    1   <Q>    1    2    5    4    </Q>
    2   <Q>    2    3    6    5    </Q>
    3   <Q>    4    5    8    7    </Q>
    4   <Q>    5    6    9    8    </Q>
</ELEMENTS>

<SURFACES NUMBER=6>
    1    1    1    <B>  w     </B>
    2    2    1    <B>  w     </B>
    3    2    2    <P>  1  4  </P>
    4    4    2    <P>  3  4  </P>
    5    4    3    <B>  v     </B>
    6    3    3    <B>  v     </B>
</SURFACES>
```

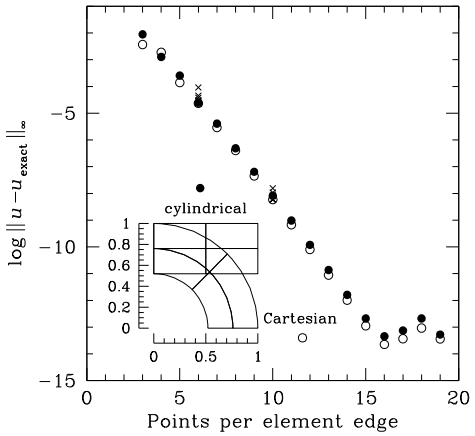


**Fig. 3.** Spatial convergence properties for spectral element simulations of Taylor–Couette flow of fluid with shear-thinning power law rheology, exponent $n = 0.6$, computed using both Cartesian and cylindrical coordinate systems and with four elements; the axial extent of the cylindrical domain was coincidentally chosen the same as its outer radius. Comparison to analytical solution. Crosses drawn for `N_P=6` and `10` show the effects in the Cartesian case of varying `REFVIS` in the range [0.2–1.8]×`PL_K` vs. 0.95×`PL_K` (value shown in listing) used for all other cases.

Note the rheology `TOKENS` for power-law fluid (see §4.1). While the constant `KINVIS` has no direct significance within `gnewt`, it is defined here partly so that the same session file might be used with the standard Newtonian solver `dns` that is part of *Semtex* to give the Newtonian-rheology result, i.e. with $n = 1$. (It is also possible to simulate the flow of Newtonian fluid using `gnewt` with power law rheology model, e.g. by setting `PL_N` = 1 in the power-law rheology tokens.)

In Fig. 3 we illustrate the spatial convergence properties of the steady solutions computed for $R_i = 0.52$ and $R_o = 1$, $w_i = 1$, $w_o = -0.5$, $n = 0.6$ in 4-element domains, both Cartesian and cylindrical. For the Cartesian simulation we have used a quarter-circle and supplied the analytical solution on the domain boundaries. As expected, the method demonstrates asymptotic exponential convergence, here down to machine-noise levels, and the outcomes for both coordinate systems are very similar. Also in Fig. 3 we illustrate the effect of substantial variation of `REFVIS` at two spatial resolution values. The effect is generally comparatively minor and less than the change associated with a variation of one order in spatial interpolation.

A Unix workflow to produce a $w$-component (azimuthal velocity) datum for Fig. 3, assuming the listing shown above is contained in text file `TC`, might be:

```
$ compare TC > TC.rst
$ gnewt TC &> /dev/null
$ compare TC TC.fld > /dev/null
Field 'u': norm_inf: 4.444e-16
Field 'v': norm_inf: 3.070e-06
Field 'w': norm_inf: 4.109e-06
Field 'p': norm_inf: 5.740e-02
Field 'l': norm_inf: 4.639e-07
```

This workflow uses the *Semtex* utility `compare` to produce from the analytical result in the `USER` section both initial conditions for `gnewt` and comparison data for the computed solution. We note that field name `l` is used for kinematic viscosity, also saved as part of the computed results.

In the session file listed above, we have used a `GROUP` that is labelled `wall`. As for *Semtex* `dns`, executing `gnewt` will create a file with an extension `.flx` to which will be written integrals of tractive forces per unit length (and, in cylindrical coordinates, moments per radian around the symmetry axis) over the `SURFACES` that are tagged into the `wall` group. See the *Semtex* user guide for more detail regarding file structure.

Here, on the (inner-radius) wall, $R_i = 0.52$, one can find from the analytical solution and rheology that $\dot{\gamma}_w = 6.07092$ and $\nu_w = 9.72139 \times 10^{-3}$. Hence one expects that the wall-generated torque per radian about the rotational axis should be $-R_i^2 \nu_w \dot{\gamma}_w L_x = -0.52^2 \times 6.0792 \times 9.72139 \times 10^{-6} \times 1 = -15.958 \times 10^{-3}$, where we have used $L_x = 1$ from the geometry; the minus sign arises because the wall rotates with a positive tangential velocity and `gnewt` computes fluid forces and moments acting on wall boundaries, rather than on the fluid.

Extracting the computed torque we find:

```
$ tail -1 TC.flx | slit -c 11
-0.0159584
```

as expected (we have used *Semtex* utility `slit` to give the last, 11th, column of `TC.flx` which contains the torque). By including the outer `SURFACES` in the `wall GROUP`, one will find the net torque is zero to a good approximation, again as expected.

### 5.2. Laminar Poiseuille flow of Carreau fluid

In [45], analytical solutions for volumetric flow rate were supplied for steady flows of GNFs with Carreau and Cross rheologies in plane and circular Poiseuille flows. An extended analytical treatment was later supplied by Wang [46] for steady Poiseuille flow of Carreau–Yasuda GNF in a circular pipe, with solutions given in terms of the Gauss hypergeometric function ${}_1F_2$. An advantage of Wang's solution over that of Sochi is that [46] provides outcomes for velocity profiles as well as for volumetric flow rate.

We have simulated the Carreau-rheology case given by Sochi in Fig. 3 (*a*) of [45] for a pressure drop of $\Delta p = 1000$ Pa over a pipe length of $L = 0.85$ m and radius $R = 0.09$ m, using a cylindrical coordinate formulation with our Carreau–Yasuda model (§4.3). As explained in [45], in order to make progress, one first needs to find the wall shear rate (or shear stress), which requires solution of a nonlinear equation since the viscosity is a function of strain rate; such requirements are common when dealing with Poiseuille flows of GNFs. The supplied rheology parameters are $n = 0.65$, $a = 2$, $\mu_0 = 0.1$ Pa.s, $\mu_\infty = 0.005$ Pa.s, $\lambda = 1.5$ s$^{-1}$. Solving eq. (14) of [45] we find (to 6 s.f.) the wall shear rate $\dot{\gamma}_w = 5920.16$ s$^{-1}$. WLOG we can take $\rho = 1$ kg/m$^3$. Non-dimensionalizing rheology parameters for convenience at a unit maximum radius as outlined in Appendix B, using dimensional length scale $L \equiv R = 0.09$ m and velocity scale (again to 6 s.f.) $U = \dot{\gamma}_w R = 532.814$ m/s, we obtain values of Carreau–Yasuda model `TOKENS` (§4.3) as follows (again to 6 s.f. for brevity): `CAR_YAS=1`, `CY_A=2.0`, `CY_N=0.65`, `CY_LAMBDA=8880.23`, `VISC_ZERO=2.08536E-3`, `VISC_INF=104.268E-6` and a dimensionless axial body force `CONST_X=372.968E-6`. From eq. (23) of [46] we have the analytical dimensionless centreline velocity $u_{\max} = 0.45324069935$. For $\nu_{\text{ref}}$ we used half the centreline value ($\nu_0$), i.e. `REFVIS=0.5*VISC_ZERO`.

The spatial convergence outcomes for centreline flow velocity for this case are shown in Fig. 4. As expected, convergence is asymptotically exponential.

### 5.3. Laminar Poiseuille flow of power-law fluid

The examples of §§5.1 and 5.2 were benign partly because the analytical value of $\nu$ remained finite everywhere in the domain, either because $\dot{\gamma} > 0$ everywhere in §5.1 or because the Carreau–Yasuda model provides a limiting maximum viscosity for the case in §5.2, even though $\dot{\gamma} = 0$ at the pipe centreline. However, as noted in §4.1 and §4.2, the viscosity becomes singular for some rheologies when $\dot{\gamma} = 0$, which e.g. occurs on the centreline of laminar pressure-driven flow in a tube or channel. In the present case we consider body-force (or pressure-gradient) driven flow in a circular tube, radius $R$ and with body force per unit mass $G$ acting in the axial direction ($G \equiv -\partial P/\partial x$). The analytical solution with power-law fluid in this case is $u = U_{\max}[1 - (r/R)^{(n+1)/n}]$,

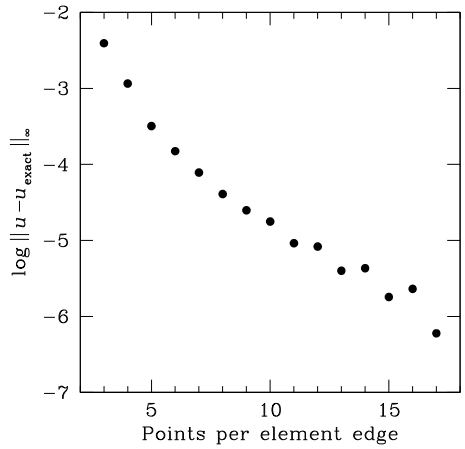


**Fig. 4.** Spatial convergence properties for spectral element simulations of circular Poiseuille flow of Carreau fluid, using a cylindrical coordinate mesh. Comparison of centreline velocity to the analytical solution of [46].

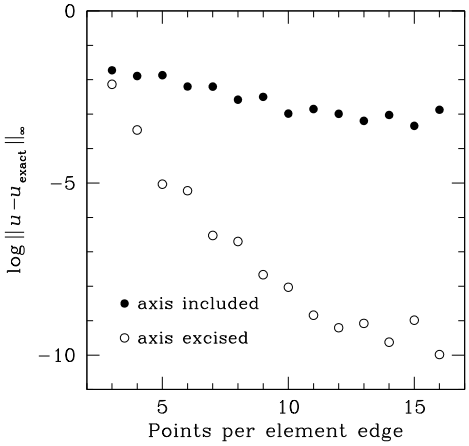


**Fig. 5.** Spatial convergence properties for spectral element simulations of Poiseuille flow of fluid with power law rheology, exponent $n = 0.6$, computed using a cylindrical coordinate system, and compared to the analytical solution. Results are shown for cases where the domain axis is included, and where the minimum radius $r_{\min} = 0.04R$.

where $U_{\max} = n/(n+1)[\rho G/(2K)]^{1/n} R^{(n+1)/n}$ (the reader may confirm that this reduces to the conventional Newtonian case for $n = 1$).

We can compute the solution in cylindrical coordinates with the axis as part of the domain (in which case we theoretically have $v = \infty$ locally, truncated numerically), or with the axis excised at some $r = r_{\min}$, where the velocity is provided by the analytical solution, and where the viscosity will remain finite (but perhaps quite large). In Fig. 5 we compare results for the two cases, with $n = 0.6$ and $r_{\min} = 0.04R$. The regularization shear rate parameter `TOKEN` was set as `PL_ZERO=1e-12`. We observe that when the axis is excised, convergence remains nearly exponential until element order becomes large, and is much more rapid than if the axis is included.

This example suggests that for rheologies for which the viscosity can theoretically become infinite where $\dot{\gamma} = 0$, the user must be cautious, especially if this can occur over an extensive region of the domain. We note, however, that if the flow is turbulent (as for examples we introduce below), this is rarely a significant issue because it is found that zero shear rates occur only very rarely (see e.g. [47] figure 6 *i–l*), and do not remain in fixed locations. Also, in such flows it is typically the case that variations in viscosity are most dynamically relevant near walls, where the shear rate is high [33,35].

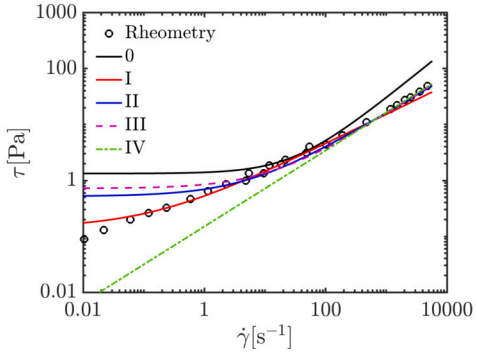


**Fig. 6.** Shear rheogram for 0.075 wt% aqueous Carbopol GNF (○), a composite of measurements made with two different rheometer types to cover a wide range of shear rates. Superimposed curves show Herschel–Bulkley (0–III) and power law (IV) model fits made over different ranges of shear rates. Re-plotted from [33].

**Table 1**
Rheology parameters fitted to the data of Fig. 6; Models 0–III are for Herschel–Bulkley rheology and IV is for power-law rheology. Note the significant variation in fitted Herschel–Bulkley rheology model parameters with shear rate range restriction.

| Model | Shear rate [$s^{-1}$] | $\tau_y$ [Pa] | $K$ [Pa $s^n$] | $n$ |
|---|---|---|---|---|
| 0 | Laminar pipe | 1.33 | 0.067 | 0.88 |
| I | 0.01–500 | 0.14 | 0.389 | 0.53 |
| II | 0.01–5000 | 0.52 | 0.177 | 0.65 |
| III | 0.01–15 000 | 0.72 | 0.129 | 0.69 |
| IV | 0.01–15 000 | – | 0.150 | 0.68 |

## 6. Validation for turbulent flow showing the importance of rheology characterization

Having demonstrated the veracity of the simulation methodology against analytical laminar solutions in §5, we now turn to DNS of turbulent flows, for which no analytical solutions exist. Validation in this case presents two difficulties: firstly, that there is a paucity of other DNS solutions with which to compare and secondly, that relevant experimental measurements of rheology are more difficult to obtain than is the case for Newtonian fluids both because GN rheology models are only low-parameter-count idealizations of real fluid behaviour and because accurate characterization of their parameter values at appropriate rates of strain is difficult to obtain.

In this section we discuss outcomes from a coupled measurement and DNS campaign where much attention was paid to the issue of rheology characterization. When attempting to fit experimentally measured rheology one should be cognizant of the range of shear rates which are liable to be important; much experimental rheological equipment can only achieve low-to-moderate shear rates, which may be much lower than could be present e.g. near the wall of a turbulent flow.

In [33] we used `gnewt` to examine rheological model characterization as applied to turbulent flow of 0.075 wt% aqueous Carbopol solution in a pipe flow rig with diameter $D = 44.5$ mm, using various models, but with rheology measurements that used two types of rheometer —concentric cylinder and parallel plate — to cover almost four orders of magnitude in shear rate. (We note that low concentration, e.g. $< 0.1$ wt%, aqueous solutions of Carbopol are generally accepted as reasonable analogs of true shear-thinning GNFs.) The rheogram and various least-squares model fits to it are shown in Fig. 6, with the parameters supplied in Table 1.

As outlined in [33], Model 0 was obtained by using the analytical solution for laminar pipe flow of Herschel–Bulkley fluid to fit $\tau_y$, $K$ and $n$ against experimental measurements of bulk velocity and pressure drop for the laminar regime in the pipe flow rig, with $\dot{\gamma}_w < 500\ s^{-1}$, see Fig. 7. Such laminar-regime pipe flow data are sometimes used for rheology

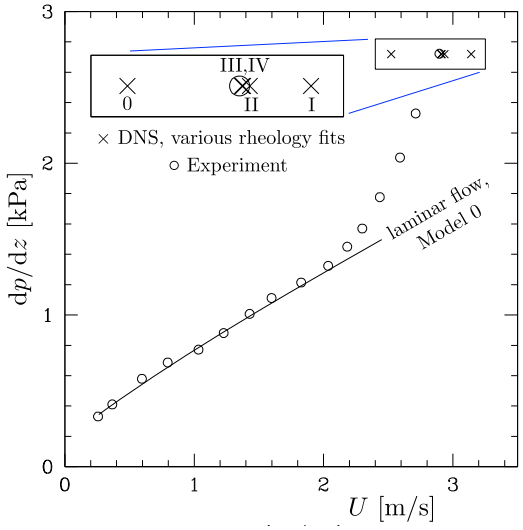


**Fig. 7.** Pressure drops and bulk velocities from the pipe loop of experiments of [33] with 0.075 wt% aqueous Carbopol solution as the working fluid, shown with turbulent DNS data for the highest pressure drop re-dimensionalized for comparative purposes. The inset shows an expanded view with labelled data corresponding to simulations with the rheology parameters from Table 1. The solid line shows the analytical laminar solution for Herschel–Bulkley fluid, fitted to provide the rheology parameters of Model 0. The onset of transition was estimated to be $U \approx 2.3$ m/s. Re-plotted from [33].

characterization of GNFs; in effect this method provides another type of rheometry. Models I–III are least-squares fits of the Herschel–Bulkley model to the rheogram over successively wider rheometer shear rate ranges, while Model IV is a power law fit over the widest shear-rate range, as for Model III. The various models provide different conditional curve fits to the true rheology, as is evident in Fig. 6; this is reflected in the differing values of the fitted constants shown in Table 1.

The different model parameters were then used as the basis for DNS studies of turbulent pipe flow. For the highest cited turbulent bulk velocity $U = Q/A = 2.90$ m/s at pressure gradient $\mathrm{d}p/\mathrm{d}z = 2720$ Pa/m (see Fig. 7) one can estimate a nominal mean wall shear rate $\dot{\gamma}_w = [(\tau_w - \tau_y)/K]^{1/n} = 2630\ \mathrm{s}^{-1}$ using the parameters of Model III and (from an elementary force balance) $\tau_w = \mathrm{d}p/\mathrm{d}z \times D/4$. This shear rate is within the fitting range of Models II–IV, but well above those used for Models 0 and I. Comparing the predicted bulk velocities to the measured value, the errors were -13.4%, 8.3%, 1.2%, 0.3% and 0.4% for Models 0–IV respectively.

These outcomes are illustrated in Fig. 7. The curve used to fit the parameters of Model 0 to the experimental data up to 2.3 m/s is also shown; as one would hope, the fit in the laminar regime is good, however, the discrepancy in predicted bulk velocity for DNS of turbulent flow using Model 0 is substantial. The discrepancy for Model I is also large. The outcomes for Models II–IV could probably all be deemed acceptable; the key point is that the upper shear rate limits of rheogram data used in fitting Models II–IV all encompass the nominal experimental maximum mean wall shear rate of 2630 $\mathrm{s}^{-1}$ whereas the upper limit used for Model I does not. Agreement between simulation and experiment is best for Models III (Herschel–Bulkley) and IV (power law), whose fitting included the same upper shear rate of 15 000 $\mathrm{s}^{-1}$.

That part of the study indicated that for acceptable accuracy in prediction of the most basic flow statistics (e.g. to within 1% on bulk velocity), the rheological modelling range should at least bracket the nominal wall shear rate, and that rheological characterization based on laminar flow in the same experimental rig is liable to be rather inadequate for the task of modelling turbulent flow.

It is notable that though Models III and IV (respectively for Herschel–Bulkley and power law rheologies, fitted over the same range of shear rates) deviate from the measured rheogram at low shear rates (substantially so for Model IV, see Fig. 6), they both match the rheogram very well at high shear rates and each predict the experimental turbulent bulk velocity to within 0.2%. This good agreement is reflected in the mean velocity profiles for Models III and IV, which are virtually indistinguishable, see Fig. 8.

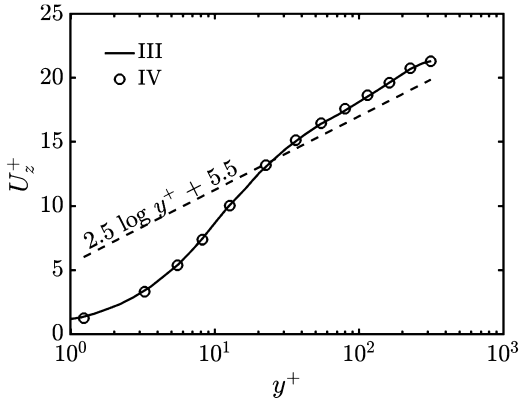


**Fig. 8.** Mean velocity profiles for Model III and IV GNF simulations corresponding to the highest experimental flow rate. Values are non-dimensionalized using the friction velocity $u^* = (\tau_w/\rho)^{1/2}$ and wall length scale $\nu_w/u^*$ in conventional fashion. Re-plotted from [33].

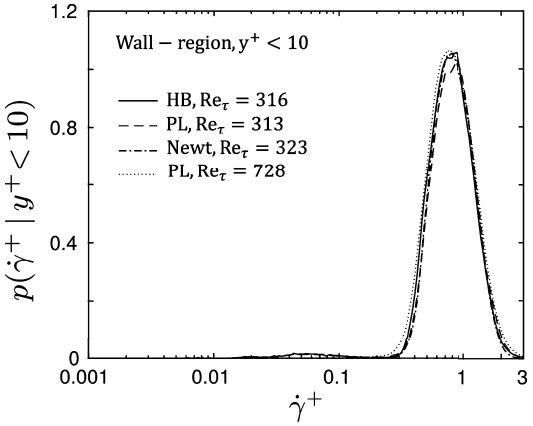


**Fig. 9.** Probability density functions of dimensionless shear rates in the near-wall region ($y^+ < 10$) for GN simulations with Models III and IV, and a matching Newtonian DNS. $\dot{\gamma}^+ = \dot{\gamma}/(u^{*^2}/\nu_w)$. Re-plotted from [33].

Based on conditional pdfs of shear rates in the wall region (see Fig. 9), we recommended that the rheological models should be fitted to at least double the maximum average nominal wall shear rate ($\dot{\gamma}^+ = 1$). Note that the near-wall shear rate pdfs for both shear-thinning GNFs are virtually indistinguishable from one another, from one obtained from a Newtonian simulation conducted at the same friction Reynolds number, and also from a simulation of power law rheology at more than twice the friction Reynolds number when expressed in wall units. Almost all the data fall below $\dot{\gamma}^+ < 2$.

Another significant outcome from [33] was that the details of the GN rheology model employed for turbulent flow studies may be relatively unimportant, provided the rheology is fitted over an appropriately large range of shear rates. For example, radial profiles of first- and second-order velocity statistics for Models III and IV were virtually indistinguishable (see Fig. 5 of [33]), even though the mean viscosity profiles differed somewhat outside the wall and buffer layers. In a later study [34], we further showed that outside the wall and buffer layers, the viscosity of a shear-thinning fluid could be held constant at the inner/outer overlap value with little effect; only the viscosity variation in the inner (near-wall) layers being very important. This observation is relevant for rheology measurements and suggests that for turbulent flow predictions

accuracy of the rheology measurements at very low shear rates where the rheology measurements are tedious and error-prone could be sacrificed in favour of high-shear-rate measurements.

The chief lesson to be drawn from this section is that DNS studies of turbulent flows of GN fluids can quite well approximate outcomes for real turbulent flows provided that the real rheology is adequately characterized at a range of shear rates relevant to turbulent flow, typically in the near-wall region.

## 7. Turbulent GN flows

In this section we briefly discuss some outcomes obtained from statistical analysis of turbulent flows of generalized Newtonian fluids in pipes, again using *Semtex*.

In [35] we examined the effect of variation in power-law index $n$ on turbulent pipe flows at $Re_\tau = u^* R/\nu_w = 323$ (bulk Reynolds numbers $O(10^4)$), keeping the wall shear stress $\tau_w$ and viscosity $\nu_w$ fixed. (The consistency $K$ was changed as $n$ was varied.) In Fig. 10 we show the effect of changing $n$ from shear thickening ($n = 1.2$) to shear thinning ($n = 0.6$) via examination of various flow statistics that may be collected by `gnewt` on setting `TOKEN AVERAGE=2`, and by using the *Semtex* utility `rstress` in post-processing to extract second-order statistics.

Fig. 10 (*a*) shows that shear thinning acts to increase the axial flow velocity at all radii (and conversely that shear thickening reduces it). Since the wall shear stress and viscosities are fixed, this means that the generalized Reynolds number $Re_G = UD/\nu_w$ increases and that the (Fanning) friction factor $f = \tau_w/(\frac{1}{2}\rho U^2)$ decreases with increasing shear thinning; shear thinning is drag reducing.

Fig. 10 (*b*) shows that in the viscous sublayer ($y^+ < 10$) the average viscosity is almost constant with distance from the wall, but then that there is significant variation with flow index and distance from the wall. An interesting side-effect (see inset) is that, for the same $\tau_w$, the mean viscosity at the wall in fact increases somewhat with shear thinning. This comes about because the average shear stress in turbulent GN flow has an additional component owing to the correlation between fluctuations in viscosity and shear rate, which is negative for shear thinning, and which, unlike Reynolds shear stress, does not fall to zero at the wall. This also implies that in the viscous sublayer, mean velocity profiles for different values of $n$ do not exactly collapse when conventional law-of-the-wall scaling is used; this may just be seen on close examination of Fig. 10 (*a*). See [35] for a more extended discourse.

Figs. 10 (*c, d*) illustrate the fact that shear thinning leads to an enhancement in streamwise velocity fluctuations and a reduction in radial (and, not shown, azimuthal) velocity fluctuations; thus, near the wall, it enhances the anisotropy of flow structure variation.

In [36] we examined the effect of changing the yield stress $\tau_y$ on turbulent flows of Bingham fluids (see §4.2) again at $Re_\tau = 323$, and again with $\tau_w$ and $\nu_w$ fixed. (We note that the shear rates were everywhere large enough that all regions were predicted to be yielded.) While there are differences in detail compared to the outcomes of [35], increasing yield stress in the rheological model had a broadly similar effect to shear thinning in that it brought about drag reduction. However, unlike power-law index variation, the effects of yield stress variation were strongest outside of the wall layers because within the wall layers, the fluid had almost pure Newtonian rheology.

## 8. An example of scaling to simulate experimental results

A recent experiment [48] examines transitional and turbulent flows of shear-thinning GN fluids in a pipe. The provided data on rheology, Reynolds number and pressure drop enables us to show how to use such experimental results to set up a simulation-based comparison. While [48] studied symmetry-breaking transitions over a wide range of Reynolds numbers, an in-depth comparison would take us too far afield and we focus on a single case near the upper end of their Reynolds number range for which the flow is turbulent.

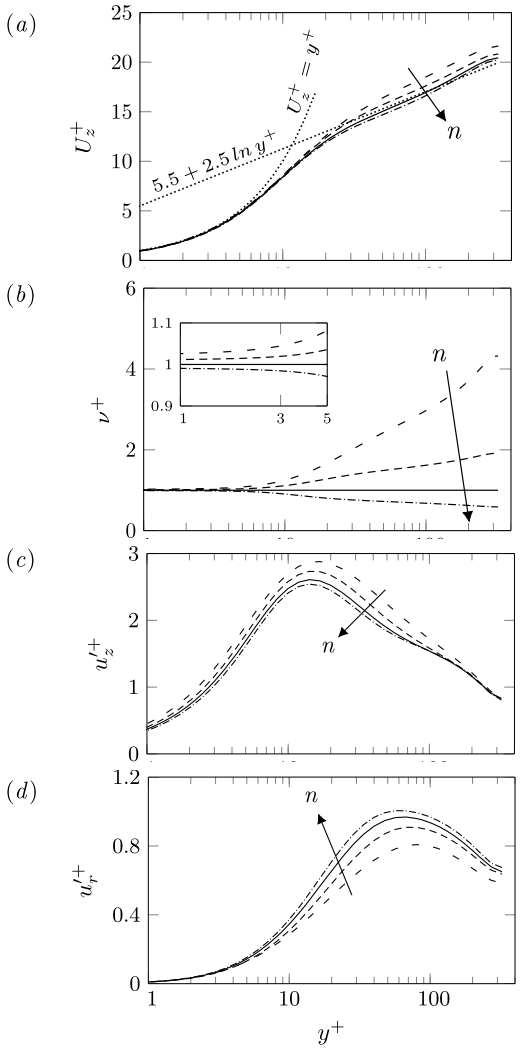


**Fig. 10.** The effect of varying flow index $n$ for turbulent pipe flows of power law GNFs, at fixed $Re_\tau = 323$. Arrows show sense of increasing $n$ from 0.6 to 1.2; solid lines are for Newtonian fluid, $n = 1$. Dimensionless profiles of (from *a–d*): average streamwise velocity, average viscosity, rms axial ($z$) and radial ($r$) velocity fluctuations. From [35].

The experiments used low-concentration aqueous solutions of Carbopol, which as we noted in §6 are commonly accepted as having quite pure GN rheologies with negligible viscoelastic effects. The case we examine used 0.08 wt% Carbopol, for which (their Table 1) a Herschel–Bulkley model was chosen, with yield stress $\tau_y = 0.06$ Pa, consistency $K = 0.23$ Pa s$^n$, and power-law index $n = 0.61$. In the experiment, pressure drop ($\Delta p$) and bulk flow velocity were measured over a 3 m length ($l$) of 25 mm diameter pipe ($D$). In their Fig. 2, flow measurement results are presented in the form of generalized Reynolds number

$$Re_G = \frac{4\rho U[(\tau_w - \tau_y)/K]^{1/n}}{\Delta p/l} \equiv \frac{UD}{\nu_w}, \tag{16}$$

with the wall viscosity derived from the wall shear stress via the rheology model, and the friction factor $f = \tau_w/(\frac{1}{2}\rho U^2)$. We assume $\rho = 1000$ kg/m$^3$.

Choosing a case they cite as turbulent, $Re_G = 8000$, we estimate $f = 0.0056$ from their Fig. 2 and then solve (16) iteratively to find $\tau_w = 30.05$ Pa from which $\Delta p/l = 4808$ Pa/m, $U = 3.276$ m/s and $\mu_w = 10.24 \times 10^{-3}$ Pa s follow. In addition the wall shear rate $\dot\gamma_w = 2935$ s$^{-1}$, cf. Fig. 6 above. Using the methodology introduced in Appendix B with $L \equiv D$ as the length scale, one obtains dimensionless rheology val-

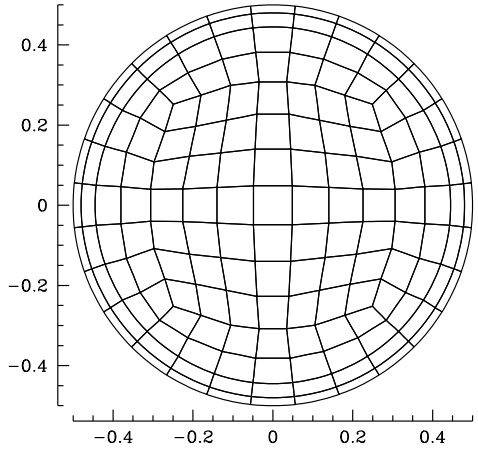


**Fig. 11.** Spectral element mesh with 161 elements used for computation of turbulent GN flow in a pipe matching a case from [48]. A session file containing this mesh can be found in `mesh/circle161` in the *Semtex* distribution.

ues $\tau'_y = 5.590\times10^{-6}$ and $K' = 419.4\times10^{-6}$, with a dimensionless body force $f' = 11.20\times10^{-3}$ to drive the flow. The nominal dimensionless average wall kinematic viscosity is $\nu'_w = 125.0\times10^{-6}$.

To compute the flow in Cartesian coordinates, we have modified a 161-element session file available as `mesh/circle161` within the *Semtex* distribution. The element outlines for this mesh, with $D = 1$, are shown in Fig. 11. The only significant changes required to the supplied session file are in the `TOKENS` section, as shown below. The reader should be able to identify the dimensionless parameters given above within the `TOKENS`. Fourier expansions are used in the $z$ (out-of-plane) dimension, with fundamental wavenumber `BETA=1` to make the streamwise domain length $L_z/D = 2\pi/\beta = 2\pi$.

```
<TOKENS>
    HB           = 1
    HB_ZERO      = 1e-8
    HB_K         = 419.4e-6
    HB_N         = 0.61
    YIELD_STRESS = 5.590e-6

    WALLVIS = 125.0e-6
    REFVIS  = 5*WALLVIS
    dpdz    = 11.20e-3

    N_TIME  = 2
    N_P     = 9
    N_Z     = 128
    BETA    = 1

    D_T     = 0.001
    T_FINAL = 100
    N_STEP  = int(T_FINAL/D_T)
    IO_CFL  = 50
    IO_FLD  = 500

    AVERAGE = 2

#   SVV_EPSZ = 20*REFVIS
#   SVV_MZ   = int(N_Z/8)
#   SVV_EPSN = 5*REFVIS
#   SVV_MN   = int(N_P/2)
</TOKENS>

<FORCE>
    CONST_Z = dpdz
</FORCE>
```

Also one may note spectral vanishing viscosity (SVV) parameter `TOKENS` [49], which are commented out — these were used to control the transition from the initially computed two-dimensional flow to a three-dimensional turbulent state; once transition completed, SVV was switched off, but we have displayed the commented-out values as an indication of what might be required to control transition (the transition process itself not being of interest here). See a more complete discussion on the use of SVV and transition control in the *Semtex* user guide within the distribution [2].

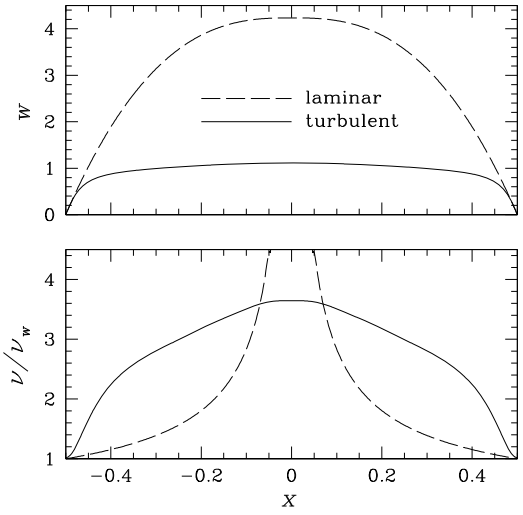


**Fig. 12.** Profiles of (upper) axial velocity and (lower) GN viscosity across the pipe for the case investigated in §8, illustrating the differences between laminar and turbulent flow.

The flow was initially computed as two-dimensional three-component with `N_Z=1`, then projected to three-dimensional three-component with `N_Z=128`, with white noise added using the `noiz` utility provided with the *Semtex* distribution to initiate transition (and with SVV enabled). After monitored energy in Fourier modes (saved in file `session.mdl`) showed that the outcome was statistically stationary, SVV was disabled. After 10 more domain wash-through times had elapsed, temporal averaging was initiated (here, with `AVERAGE=2` to allow computation of Reynolds stress terms as well as averages of primitive variables and viscosity) for approximately 30 domain wash-through times (in two tranches of 100 time units). These procedures are all documented in the *Semtex* user guide. To run the GN solver in parallel via MPI, one uses the `gnewt_mp` executable as below (where the session file name used was `HB03`, and 16 processes are employed):

```
$ mpirun -n 16 gnewt_mp HB03
```

We note that while a zero-shear-rate regularization cutoff (`HB_ZERO`) has been supplied (as is potentially appropriate to computations with power law or Herschel–Bulkley rheologies), checks of instantaneous field file dumps written out during execution in the turbulent regime showed that at no point in the mesh did the shear rate in fact drop to be close to supplied cut-off value $\dot\gamma = 1\times10^{-8}$, in line with our remarks at the end of §5.3. For example, using one representative field dump from the turbulent regime, we can use *Semtex* utilities first to add the rate-of-strain field (labelled `g` below), and then find its maximum and minimum values:

```
$ addfield -g -s HB03 HB03.fld > tmp.fld
$ fpminmax.py tmp.fld
             MIN           MAX
u      -0.25175      0.324007
v      -0.23658      0.222059
w    -0.0220225       1.20063
p     -0.033499     0.0425688
l   6.57495e-05    0.00129744
g     0.0671788        114.77
```

Reassuringly, we observe that the minimum reported instantaneous value for $\mathtt{g} \equiv \dot\gamma = 0.0671788$, much larger than the supplied minimum cut-off value of `HB_ZER0=1e-8`.

In Fig. 12 we show comparisons of axial velocity and GN viscosity profiles obtained in laminar and turbulent flow simulations for this case.

(Data for the turbulent flow were first averaged in time, then axially and azimuthally.) The wall viscosity $\nu_w$ for the laminar flow matched the expected value of $125.0\times10^{-6}$ to 4 s.f., whereas for the turbulent flow the average value of $\nu_w = 127.1\times10^{-6}$, or 1.7% higher (for the same value of $\tau_w$, a somewhat larger average value of viscosity will be obtained at the wall for turbulent vs. laminar flow of the same shear-thinning GNF, see discussion in §7 above). As expected, the centreline viscosity becomes very large in the laminar case — the theoretically infinite laminar centreline value for Herschel–Bulkley fluid cannot of course be adequately resolved by the simulation, though this has little influence on the velocity profile. The mean centreline streamwise velocity in the turbulent regime is observed from Fig. 12 to be approximately 1.1, in line with the instantaneous maximum $\mathrm{w} = 1.20063$ reported above.

Computing the bulk flow velocities, we find that for laminar flow $Re_G = 19.3\times10^3$, while for turbulent flow, $Re_G = 6890$, the latter being significantly (13.8%) smaller than the experimentally nominated value of $Re_G = 8000$. One naturally expects some variation owing to the comparatively coarse (2 s.f.) estimate of $C_f = 0.0056$ we extracted from figure 2 of [48], the fact that the supplied rheology parameters were also given to 2 s.f., the possibility that the Reynolds number is low enough that the flow is still transitional (hence, sensitive) and to possible influences of domain size and numerical resolution (both of which we believe are adequate).

However, as discussed in §6, such a large variation between experimental and computed bulk velocities could also result from having fitted the rheological model parameters to rheological data obtained over a restricted range of shear rates, compared to values relevant to those which may occur at the wall in a turbulent flow. From our previous analyses (§6) we would recommend that for the equipment used, shear rates of up to 6000 $\mathrm{s}^{-1}$ should be obtained to characterize the rheology adequately for DNS accuracy at $Re_G = 8000$. Based on the descriptions of rheological equipment in [48], we believe that this is unlikely to have been achieved.

## 9. Discussion and conclusion

There are many rheology models available for GNFs (see [6]). They encompass fluids that are shear-thinning, shear-thickening, fluids with a yield stress and those with low and/or high strain rate plateaus. A very important consideration when using these rheology models is that there is usually no underlying fundamental physical theory to suggest that they correctly describe the rheology of any known fluid across all shear rates. They have largely been developed empirically based on experimental measurements of shear stress versus strain rate (commonly termed a rheogram), usually over a limited range of shear rates. As such, they are simply fits to the data. As shown in [33], and here in §6, rheology data used to fit the model parameters must cover the range of shear rates of relevance for a simulation, otherwise the fit can be significantly in error in important regions of the flow, especially near solid boundaries where strain rates are typically high, for example in a turbulent flow. It is notable that while low-shear-rate parameter fits may be wholly adequate for laminar flow solutions, they can lead to significant errors when employed for turbulent flows where high shear rates are important in controlling dynamics, cf. Fig. 7.

The methodology generally possesses the exponential spatial convergence properties that one expects of high order methods, see §§5.1, 5.2, and temporal convergence at orders 1–3, see §Appendix A. For some laminar flow calculations with power law or Herschel–Bulkley rheologies and where the shear rate may reach zero somewhere in the domain (e.g. at the centre of Poiseuille flows in pipes or channels, see §5.3) it may be advisable to use viscosity regularization (cut-off on minimum numerical shear rate) to avoid theoretically infinite viscosity in these locations. The local accuracy of simulation predictions in such regions depends somewhat on the cut-off shear rate specified for the simulation. However, in turbulent flow calculations using such symmetric geometries, this issue is generally not significant. The shear rate rarely approaches zero, and even if it does, this is only likely to occur near the centre, where detail of viscosity variation has only minor influence on turbulent flow predictions [34].

In this article, we have outlined the numerical methodology and capabilities of the GN solver extension of *Semtex*, `gnewt`, and provided best practices for simulating the flow of generalized Newtonian fluids. The distribution includes commonly used GN rheology models, and the solver is designed to be readily extensible to others. New rheology models can be easily incorporated by modifying a single source file, `viscosity.cpp`. While *Semtex* supports solving the Navier–Stokes equations and scalar transport for Newtonian fluids, the GN extension is currently limited to solving only the Navier–Stokes equations. Future work will focus on extending the `gnewt` solver to include scalar transport equations. This will enable studies on heat transfer in GNFs and the modeling of viscosity as a function of fine particle concentration under the continuum assumption.

## CRediT authorship contribution statement

**H.M. Blackburn:** Writing – original draft, Supervision, Software, Methodology, Formal analysis, Data curation, Conceptualization. **M. Rudman:** Writing – original draft, Validation, Formal analysis, Conceptualization. **J. Singh:** Writing – original draft, Software, Investigation, Conceptualization.

## Declaration of competing interest

The authors declare that they have no known competing financial interests or personal relationships that could have appeared to influence the work reported in this paper.

## Appendix A. Temporal accuracy of the time-integration scheme

In §3 we explained that owing to the appearance of some viscous terms in (11) which are not amenable to the rotational-form decomposition of (10), the velocity-correction scheme (6)–(9), (11) does not conform to the standard rotational form described in [41–43]. Hence one may be concerned that the temporal accuracy of the method is compromised. For testing of temporal convergence it is adequate to consider Stokes flow [43].

Since it is the decomposition of viscous stress in (4) rather than the dependence of viscosity on $\dot\gamma$ which is the main point in question, we carry out tests for which $\nu = \text{const.}$, i.e. Newtonian rheology; the test case is decaying Stokes flow in a channel, for which an analytical solution exists, see [41] §3.1. We examine the decay rate $\sigma$ of the solution for $\nu = 1$. Computations were carried out using 24 quadrilateral elements with GLL polynomial order $N_P = 15$ to span the domain $[-\pi,+\pi]\times[-0.5,+0.5]$ (i.e. errors are dominated by the temporal discretization). Convergence of $\sigma$ w.r.t. $\Delta t$ are shown in Fig. 13. Outcomes for the standard Newtonian solver described in [1] are shown as open symbols; these confirm the expected convergence rates for time orders $K = 1,2,3$.

For testing temporal behaviour of the GN solver we take the approach of setting $\boldsymbol{N} = 0$, $\nu_{\mathrm{ref}} = 1+\delta$, $\nu = 1$ so that in (6), $\nu - \nu_{\mathrm{ref}} = -\delta$; the viscous decomposition (4) is still in force, but unsteady Stokes flow is computed with an overall viscosity level $\nu = 1$. Outcomes are shown as filled symbols in Fig. 13; one may observe that the temporal convergence properties closely match those for the standard Newtonian solver. For $K = 1,2$, $\delta = 1$ (large compared to unity), while for $K = 3$ (which is not A-stable in the Newtonian case, see [41]), $\delta = 0.1$; if $\delta$ was made too large for $K = 3$, stability and accuracy were compromised. These results suggest that even though (6)–(9), (11) does not strictly conform to rotational form, the formal temporal accuracy of the original method is retained if the simulations are stable. We note that the default time-order for the code is $K = 2$; $K = 3$ is rarely used in practice (owing to typical relationships between CFL limits and spatial accuracy).

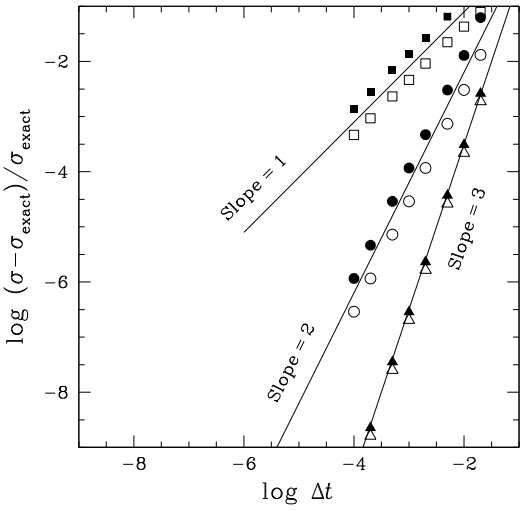


**Fig. 13.** Temporal convergence properties of the fractional step scheme for time orders $K = 1, 2, 3$, carried out for decaying Stokes flow in a channel with eigenvalue $\sigma$, see text and [41], §3.1. Open symbols are for the standard Newtonian solver described in [1], filled symbols are for the GN solver, with nonlinear advection terms disabled.

## Appendix B. Non-dimensionalization of rheological parameters

Rheology model parameters for real fluids are invariably established experimentally and are typically supplied in dimensional form. For simulations however, it is more usual to consider dimensionless forms, and to have velocity and length scales of order unity. Hence one often needs to convert rheology model parameters to dimensionless form, and here we discuss one way to approach this task. We use the velocity scale $U$ and length scale $L$ (in a pipe flow experiment, these might be the bulk velocity and pipe diameter), as well as density $\rho$.

Terms in the momentum equations of (2) all have dimensions of force per unit volume. Simplifying notation to scalar quantities, we can consider the nonlinear terms, the pressure gradient, the viscous terms and body force terms to be of forms $\rho\partial(u^2)/\partial x$, $\partial p/\partial x$, $\partial(\mu\partial u/\partial x)/\partial x$ and $\rho f$ respectively. Now consider dimensionless quantities such as $x' = x/L$, $u' = u/U$. Then $\rho\partial(u^2)/\partial x \to (\rho U^2/L)\partial u'^2/\partial x'$, $\partial p/\partial x \to (U^2/L)\partial p'/\partial x'$, $\partial(\mu\partial u/\partial x)/\partial x \to (U/L^2)\partial(\mu\partial u'/\partial x')/\partial x'$ and $\rho f \to (\rho U^2/L)f'$. Dividing each term by $\rho U^2/L$ we obtain $\partial u'^2/\partial x'$, $\rho^{-1}\partial p'/\partial x' \equiv \partial P'/\partial x'$, $(\rho U L)^{-1}\partial(\mu\partial u'/\partial x')/\partial x'$ and $f'$. (Note the appearance here of the 'kinematic pressure' $P = p/\rho$, very often used unremarked in place of pressure for incompressible simulations, those of *Semtex* included.)

From the above one arrives at the dimensionless kinematic viscosity $\nu' = \mu/(\rho U L)$, i.e. $(\rho U L)^{-1}\partial(\mu\partial u'/\partial x')/\partial x' \to \partial(\nu'\partial u'/\partial x')/\partial x'$. To make further progress, one must examine the particular functional form of $\mu = \mu(\dot\gamma)$, since $\dot\gamma = (U/L)\dot\gamma'$. As an example, for Herschel–Bulkley rheology (§4.2), we obtain $\tau_y' = \tau_y/(\rho U^2)$ and $K' = KU^{n-2}/\rho L^n$.

## Data availability

Data will be made available on request.

## References

[1] H.M. Blackburn, D. Lee, T. Albrecht, J. Singh, Semtex: a spectral element–Fourier solver for the incompressible Navier–Stokes equations in cylindrical or Cartesian coordinates, Comput. Phys. Commun. 245 (2019).
[2] H.M. Blackburn, Semtex release 11 (source code), https://gitlab.com/semtex-base/semtex, 2025.
[3] H.M. Blackburn, S.J. Sherwin, Formulation of a Galerkin spectral element–Fourier method for three-dimensional incompressible flows in cylindrical geometries, J. Comput. Phys. 197 (2004) 759–778.
[4] R.D. Henderson, G.E. Karniadakis, Unstructured spectral element methods for simulation of turbulent flows, J. Comput. Phys. 122 (1995) 191–217.
[5] R.B. Bird, Useful non-Newtonian models, Annu. Rev. Fluid Mech. 8 (1976) 13–34.
[6] R.P. Chhabra, J.F. Richardson, Non-Newtonian Flow and Applied Rheology, 2nd ed., Elsevier, 2008.
[7] L. Pullum, D.V. Boger, F. Sofra, Hydraulic mineral waste transport and storage, Annu. Rev. Fluid Mech. 58 (2018) 157–185.
[8] S. Akhshik, M. Behzad, M. Rajabi, CFD–DEM approach to investigate the effect of drill pipe rotation on cuttings transport behavior, J. Pet. Sci. Eng. 127 (2015) 229–244.
[9] T.J. Pedley, The Fluid Mechanics of Large Blood Vessels, Cambridge University Press, 1980.
[10] B.M. Johnston, P.R. Johnston, S. Corney, D. Kilpatrick, Non-Newtonian blood flow in human right coronary arteries: transient simulations, J. Biomech. 39 (2006) 1116–1128.
[11] S.N. Doost, L. Zhong, B. Su, Y.S. Morsi, The numerical analysis of non-Newtonian blood flow in human patient-specific left ventricle, Comput. Methods Programs Biomed. 127 (2016) 232–247.
[12] A.N. Beris, R. Sureskumar, Pseudospectral simulation of turbulent viscoelastic channel flow, Chem. Eng. Sci. 51 (1996) 1451–1471.
[13] R. Sureskumar, A.N. Beris, A.H. Handler, Direct numerical simulation of the turbulent channel flow of a polymer solution, Phys. Fluids 9 (1997) 743–755.
[14] C.D. Dimitropoulos, R. Sureshkumar, A.N. Beris, Direct numerical simulation of viscoelastic turbulent channel flow exhibiting drag reduction: effect of the variation of rheological parameters, J. Non-Newton. Fluid Mech. 79 (1998) 433–468.
[15] A.N. Beris, C.D. Dimitropoulos, Pseudospectral simulation of turbulent viscoelastic channel flow, Comput. Methods Appl. Mech. Eng. 180 (1999) 365–392.
[16] M. Rudman, H.M. Blackburn, L.J.W. Graham, L. Pullum, Turbulent pipe flow of non-Newtonian fluids, J. Non-Newton. Fluid Mech. 118 (2004) 33–48.
[17] T. Ohta, M. Miyashita, DNS and LES with an extended Smagorinsky model for wall turbulence in non-Newtonian viscous fluids, J. Non-Newton. Fluid Mech. 206 (2014) 29–39.
[18] A.A. Gavrilov, V.Y. Rudyak, Direct numerical simulation of the turbulent energy balance and the shear stresses in power-law fluid flows in pipes, Fluid Dyn. 52 (2017) 363–374.
[19] A.A. Arosemena, R. Andersson, H.I. Andersson, J. Solsvik, Effects of shear-thinning rheology on near-wall turbulent structures, J. Fluid Mech. 925 (2021) A37.
[20] C. Narayanan, J. Singh, S. Nauer, R. Belt, T. Palermo, D. Lakehal, Turbulent flow of non-Newtonian fluid in rough channels, J. Fluid Mech. 1000 (2024) A55.
[21] E.Z. Zheng, M. Rudman, J. Singh, S.B. Kuang, Direct numerical simulation of turbulent non-Newtonian flow using OpenFOAM, Appl. Math. Model. 72 (2019) 50–67.
[22] D.T. Karahan, D. Ranjan, C.K. Aidun, Turbulent channel flow of generalized Newtonian fluids at $\mathrm{Re}^\tau = 180$, J. Non-Newton. Fluid Mech. 314 (2023) 105015.
[23] F.O. Basso, A.T. Franco, Numerical investigation of turbulent flow of Herschel—Bulkley fluids in a concentric annulus with inner cylinder rotation, J. Non-Newton. Fluid Mech. 327 (2024) 105219.
[24] V.L. Marrero, J.A. Tichy, O. Sahni, K.E. Jansen, Numerical study of purely viscous non-Newtonian flow in an abdominal aortic aneurysm, ASME J. Biomech. Eng. 136 (2014) 101001.
[25] M. Mortensen, K. Valen-Sendstad, Oasis: a high-level/high-performance Navier–Stokes solver, Comput. Phys. Commun. 188 (2015) 177–188.
[26] M.O. Kha, K. Valen-Sendstad, D.A. Steinman, Direct numerical simulation of laminar-turbulent transition in a non-axisymmetric stenosis model for Newtonian vs. Shear-thinning non-Newtonian rheologies, Flow Turbul. Combust. 102 (2019) 43–72.
[27] R. Schussnig, D.R.Q. Pacheco, T.-P. Fries, Robust stabilized finite element solvers for generalised Newtonian fluid flows, J. Comput. Phys. 442 (2021) 110436.
[28] D. Bošnjak, R. Schussnig, S. Ranftl, G.A. Holzapfel, T.-P. Fries, Geometric uncertainty of patient-specific blood vessels and its impact on aortic hemodynamics: a computational study, Comput. Biol. Med. 190 (2025) 110017.
[29] P.F. Fischer, Nek5000 (source code), https://github.com/Nek5000/Nek5000, 2025.
[30] X. Chen, Y.M. Chung, M. Wan, The statistical characteristics and auto-regeneration of backflow in non-Newtonian turbulent pipe flow, Phys. Fluids 36 (2024) 025121.
[31] M. Rudman, H.M. Blackburn, Direct numerical simulation of turbulent non-Newtonian flow using a spectral element method, Appl. Math. Model. 30 (2006) 1229–1248.
[32] J. Singh, M. Rudman, H.M. Blackburn, A. Chryss, L. Pullum, Turbulent flow of non-Newtonian fluids in a partially blocked pipe, in: 19 A/Asian Fluid Mech. Conf., Melbourne, 2014.
[33] J. Singh, M. Rudman, H.M. Blackburn, A. Chryss, L. Pullum, L.J.W. Graham, The importance of rheology characterization in predicting turbulent pipe flow of generalized Newtonian fluids, J. Non-Newton. Fluid Mech. 232 (2016) 11–21.
[34] J. Singh, M. Rudman, H.M. Blackburn, The rheology dependent region in turbulent pipe flow of a generalised Newtonian fluid, in: 20 A/Asian Fluid Mech. Conf., Perth, 2016.
[35] J. Singh, M. Rudman, H.M. Blackburn, The influence of shear-dependent rheology on turbulent pipe flow, J. Fluid Mech. 822 (2017) 848–879.
[36] J. Singh, M. Rudman, H.M. Blackburn, The effect of yield stress on pipe flow turbulence for generalised Newtonian fluids, J. Non-Newton. Fluid Mech. 249 (2017) 53–62.
[37] M. Rudman, J. Singh, H.M. Blackburn, Turbulent flow of shear-thinning slurries in a flume, in: 20 Int. Conf. Hydrotrans., Melbourne, 2017.

[38] D.C. Leslie, S. Gao, The stability of spectral schemes for the large eddy simulation of channel flows, Int. J. Numer. Methods Fluids 8 (1988) 1107–1116.
[39] G. Barrenechea, E. Castillo, D. Pacheco, Implicit-explicit schemes for incompressible flow problems with variable viscosity, SIAM J. Sci. Comput. 46 (2024) A2660–A2682.
[40] G. Dahlquist, Å. Björck, Numerical Methods, Prentice-Hall, 1974. Dover edition, 2003.
[41] G.E. Karniadakis, M. Israeli, S.A. Orszag, High-order splitting methods for the incompressible Navier–Stokes equations, J. Comput. Phys. 97 (1991) 414–443.
[42] J.L. Guermond, J. Shen, Velocity-correction projection methods for incompressible flows, SIAM J. Numer. Anal. 41 (2003) 112–134.
[43] J.L. Guermond, P. Minev, J. Shen, An overview of projection methods for incompressible flows, Comput. Methods Appl. Mech. Eng. 195 (2006) 6011–6045.
[44] G.E. Karniadakis, S.J. Sherwin, Spectral/$hp$ Element Methods for Computational Fluid Dynamics, 2nd ed., Oxford University Press, 2005.
[45] T. Sochi, Analytical solutions for the flow of Carreau and cross fluids in circular pipes and thin slits, Rheol. Acta 54 (2015) 745–756.
[46] Y. Wang, Steady isothermal flow of a Carreau–Yasuda model fluid in a straight circular tube, J. Non-Newton. Fluid Mech. 310 (2022).
[47] H.M. Blackburn, N.N. Mansour, B.J. Cantwell, Topology of fine-scale motions in turbulent channel flow, J. Fluid Mech. 310 (1996) 269–292.
[48] A. Charles, J. Peixinho, T. Ribeiro, V. Rocher, J.-C. Baudez, S.A. Bahrani, Asymmetry and intermittency in the rheo-inertial transition to turbulence in pipe flow, Phys. Fluids 36 (2004) 054120.
[49] K. Koal, J. Stiller, H.M. Blackburn, Adapting the spectral vanishing viscosity method for large-eddy simulations in cylindrical configurations, J. Comput. Phys. 231 (2012) 3389–3405.